Scattering to Higher Harmonics for Quarter Wave and Helmholtz Resonators

K. Förner, J. Tournadre†‡, P. Martínez-Lera†, and W. Polifke

Professur für Thermofluiddynamik, Technische Universität München
Boltzmannstr. 15, 85748 Garching b. München, Germany

†Siemens Industry Software
Researchpark 1237, Interleuvenlaan 68, 3001 Leuven, Belgium

‡KU Leuven, Dept. of Mechanical Engineering
Celestijnenlaan 300B, 3001 Leuven, Belgium

The nonlinear response of acoustic resonators is investigated over a broad range of frequencies and amplitudes. Helmholtz resonators with a symmetric and with an asymmetric neck, respectively, as well as quarter wave resonators are considered. Describing functions for impedance and reflection coefficient of a Helmholtz resonator at various sound pressure levels are determined from compressible flow simulation and validated against experimental data. The particular focus of the present study is the nonlinear scattering to higher harmonics. For the Helmholtz resonator with a symmetric neck, a distinct pattern in the amplitudes of the higher harmonics is observed, where the odd harmonics dominate the response, while the even harmonics are almost negligible. Such an "Odd-Harmonics-Only" (OHO) pattern, which was observed previously in experiment at orifices, can be explained by a quasi-steady analysis based on the Bernoulli equation, assuming a symmetric flow pattern at the neck. For the Helmholtz resonator with an asymmetric neck, it is observed in CFD simulations that even harmonics contribute noticeably to the resonator response, such that the OHO pattern is less pronounced. For the markedly asymmetric geometry of the quarter wave resonator, the second harmonic is dominant and the OHO pattern vanishes completely. The quasi-steady analysis is extended successfully to describe also nonlinear scattering to higher harmonics for asymmetric configurations and flow patterns. Overall, the scattering to higher harmonics remains on a moderate level even at very high excitation levels for the Helmholtz resonator configurations. For the quarter wave resonator, the scattering is more pronounced and contributes perceptibly to the response at high excitation amplitudes.

Nomenclature

A_f, A_u Input amplitudes, m/s
c_0 Speed of sound, m/s
C_d Contraction factor, –
d_0 Neck diameter and quarter wave resonator diameter, m
d_{cav} Back-cavity diameter, m
f, g Riemann invariants, m/s
f_0 Fundamental frequency, Hz
f_{res} Resonator eigenfrequency, Hz
l_0 Neck thickness and quarter wave resonator length, m

American Institute of Aeronautics and Astronautics

l_{cav}	Back-cavity length, m
l_{ch}	Chamfer length, m
l_e	Effective length, m
p	Pressure, Pa
R	Reflection coefficient, –
t	Time, s
u'	Fluctuating velocity in the resonator tube, m/s
u'_o	Fluctuating velocity in the neck, m/s
Z, z	Acoustic impedance (non-normalized and normalized), Rayl/–

Conventions

OHO	"Odd-harmonics-only" pattern
SPL	Sound pressure level, dB

Symbols

Δp	Pressure loss, Pa
ω_0	Fundamental angular frequency, rad/s
ω_{res}	Resonator angular eigenfrequency, rad/s
ϕ	Acoustic velocity potential, m^2/s
ρ_0	Density, kg/m^3
σ	Open area ratio, –

Superscripts

$\bullet^{AJ}$	quantity corresponding to the area jump
$\hat{\bullet}$	Fourier transformed variable
$\bullet'$	Acoustic fluctuating part of the variable

I. Introduction

Preprint

$\mathbf{A}$COUSTIC resonators are used in various industrial applications to reduce sound emission or to avoid thermoacoustic instabilities. The basic types of such resonators are the Helmholtz and the quarter wave resonators, which are sketched in Fig. 1.

It is well known that the acoustic response of such resonators becomes nonlinear at sufficiently high excitation amplitudes. The nonlinearities are related to flow separation at the resonator edges, which lead to an increase in the dissipation of acoustic energy, in addition to the thermo-viscous losses at the walls. For harmonic excitation, two aspects of nonlinearity can be distinguished: On the one hand, amplitude and phase of the reflected wave at the frequency of excitation may depend on the amplitude of excitation. This behaviour can be described in terms of describing functions for the resonator impedance, or its reflection coefficient, see for instance Hersh et al.[1] or the Appendix of the present paper.

On the other hand, scattering of acoustic energy to other frequencies may occur. This was investigated, e. g., by Hersh and Walker[2] for a Helmholtz resonator. The scattering to higher harmonics at an orifice, a problem which is closely related to the Helmholtz resonator, was studied experimentally and analytically by Ingard and co-workers[3,4] as well as Cummings.[5] An "Odd-Harmonics-Only" (OHO) pattern in the higher harmonics was observed, where only the odd harmonics are present in the response. This observation could be explained by a quasi-steady analysis based on Bernoulli's equation.

The present study investigates the nonlinear acoustic scattering of both Helmholtz and quarter wave resonator designs by means of CFD simulation. The occurrence of the OHO patter is found to depend on the symmetry of the configuration under study. The quasi-steady theory[4,5] is extended to also describe asymmetric configurations and flow patterns, such that it can be applied also to Helmholtz resonators with an asymmetric neck, or quarter wave resonators.

The paper is organized as follows: The approaches to describe the resonators response restricted to the fundamental frequency are presented in Sec. II. The quasi-steady theory from the literature is also introduced in this section. In Sec. III, this theory is applied for the considered cases and the scattering behavior is evaluated. Section IV presents the scattering behavior observed in the CFD simulations for both the Helmholtz and quarter wave resonators. The behavior is also compared to analytical prediction. Finally, the findings are summarized in Sec. V.
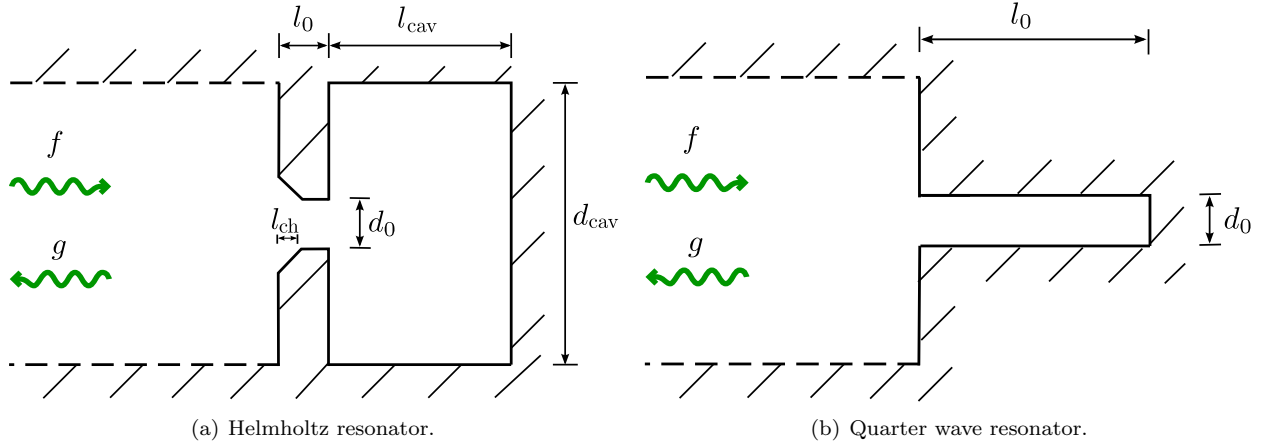
American Institute of Aeronautics and Astronautics

(a) Helmholtz resonator.

(b) Quarter wave resonator.

Figure 1. Sketch of both resonator types considered. Slip walls in the simulations are marked by dashed lines.

II. Physical Background

In this section, basic terminology to characterize acoustic resonators is introduced. Moreover, a quasi-steady analysis based on the incompressible Bernoulli equation is presented, which accounts for nonlinearities of the pressure drop across the neck of a resonator.

II.A. Impedance and Refection Coefficient Describing Functions

The behavior of an acoustic resonator is often described in the frequency domain by its *impedance Z*. It is defined as the ratio of the Fourier transforms (ˆ) of the fluctuating acoustic pressure p' and velocity u' normal to the reference surface:

$$Z(f_0) = z(f_0)\, c_0 \rho_0 = \frac{\hat{p}(f_0)}{\hat{u}(f_0)} \ . \tag{1}$$

Here, f_0 denotes the excitation frequency. The real part of the impedance is referred to as *resistance* and its imaginary part as *reactance*. In the following, impedance values normalized with the air specific impedance $\rho_0 c_0$ are denoted by z. Here, ρ_0 and c_0 stand for the mean density and the speed of sound, respectively.

The resonator can also be characterized in terms of characteristic wave amplitudes f and g, assuming 1-D acoustics in front of the resonator. These f and g quantities can be considered as right and left traveling waves, respectively. In absence of mean flow, they are defined as $f = 1/2\,(p'/(\rho_0 c_0) + u')$ and $g = 1/2\,(p'/(\rho_0 c_0) - u')$. The ratio of the reflected $\hat{g}(f_0)$ wave to the normally incident $\hat{f}(f_0)$ wave in frequency domain is referred to as the *reflection coefficient* $R(f_0) = \hat{g}(f_0)/\hat{f}(f_0)$. Its relation to the impedance is given by:

$$R(f_0) = \frac{\hat{g}(f_0)}{\hat{f}(f_0)} = \frac{Z(f_0) - \rho_0 c_0}{Z(f_0) + \rho_0 c_0} = \frac{z(f_0) - 1}{z(f_0) + 1} \ . \tag{2}$$

At the resonator eigenfrequency f_{res}, the reactance vanishes $\Im(Z(f_{\mathrm{res}})) = 0$ and, accordingly, the optimal resistance equals the specific impedance $\rho_0 c_0$ of the medium, where no reflection takes place at all (i.e., $|R(f_{\mathrm{res}})| = 0$). Thus, the gain of the reflection coefficient decreases with increasing SPL until it reaches the optimal resistance $Re(z(f_{\mathrm{res}})) = 1$. For a resistance larger than this optimal value $\Re(z(f_{\mathrm{res}})) > 1$, the resonator is called *overdamped*. In that case, the reflection coefficient grows with a further increase of the resistance as can be also observed in Sec. IV.

The concepts introduced above are not able to characterize nonlinear phenomena since Z and R do not depend on the excitation amplitude. To extend the impedance to the nonlinear regime, the describing function approach is commonly used, see for instance Hersh *et al.*,[1] which is referred to as *impedance describing function* in the following. Here, the impedance is specified not only in dependency on the frequency, but also on the excitation amplitude. This is commonly done in terms of the *sound pressure level* (SPL) present at a certain reference position. The value of this SPL is defined as $20 \log_{10}(p_{\mathrm{rms}}/p_{\mathrm{ref}})$, where p_{rms} and p_{ref} denote the root mean square of the fluctuating pressure and the reference pressure in air $20\,\mu$Pa, respectively.

(a) Orifice.
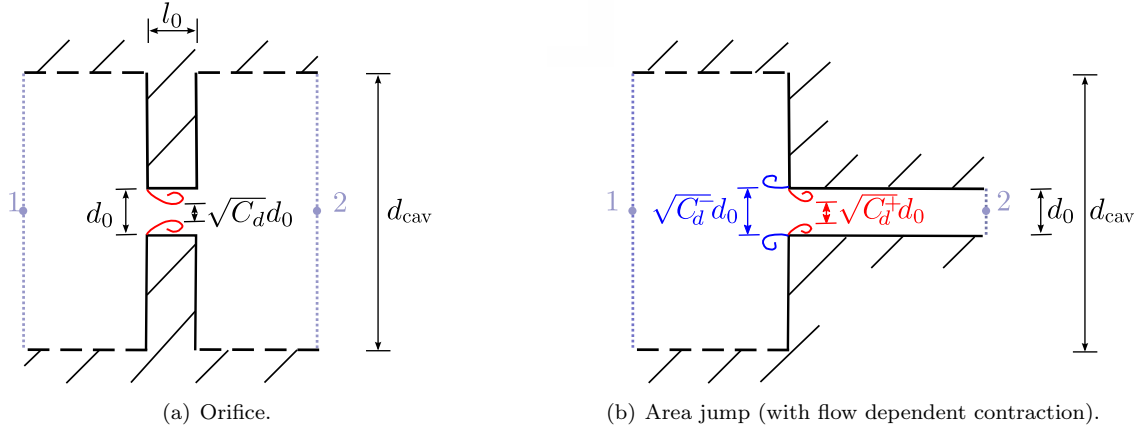
(b) Area jump (with flow dependent contraction).

Figure 2. Sketch of the corresponding geometries for the incompressible analysis.

Note that this approach cannot represent the nonlinear behavior in a comprehensive manner, but only the behavior for the fundamental frequency of excitation. In particular, the scattering to higher harmonics is not included in this describing approach, which is investigated in the current paper.

II.B.   Flow Separation as the Cause of Nonlinear Behavior

The Helmholtz resonator can be analyzed as a combination of an acoustically compact orifice and a backing volume in the linear and nonlinear regime.[6] Thus, the loss mechanisms for a Helmholtz resonator are the same as those at an orifice. To understand those mechanisms, the 1-D unsteady Bernoulli equation with suitable extensions for the loss terms can be studied for an orifice as sketched in Fig. 2(a), see, e. g., references [4], [5] and [7]. In the quarter wave resonator case, the situation is different due to the asymmetry of the area jump, as sketched in Fig. 2(b), but can be analyzed in a similar framework. The following discussion helps to understand how the nonlinear losses are caused in both configurations.

At first, the Helmholtz resonator is considered. It is assumed here that the resonator neck is acoustically compact such that it can be treated as an incompressible orifice. Viscous losses are neglected at the beginning of this consideration and the Bernoulli equation is studied. This equation reads in terms of fluctuating quantities as:

$$\frac{\partial \phi'}{\partial t} + \frac{1}{2} u'^2 + \frac{p'}{\rho_0} = \text{const. ,} \tag{3}$$

where ϕ is the potential $u' = \nabla \phi$. The equation above is integrated from position 1 to 2 sketched in Fig. 2(a). The effective length l_e is introduced to express the result in a compact form:

$$\phi'_2 - \phi'_1 = \int_1^2 u'(x) \mathrm{d}x = \int_1^2 \frac{A_o u'_o}{A(x)} \mathrm{d}x = u'_o l_e = \frac{u'}{\sigma} \, l_e \; . \tag{4}$$

Here, A_o and u'_o denote the cross section area and the velocity in the orifice, respectively. The x-dependent cross section area formed by the flow path is $A(x)$ and σ stands for the area ratio $\sigma = d_0^2/d_{\text{cav}}^2$. Note that the effective length equals the geometrical length of the orifice l_o with an additional end correction added, see, e. g., Ingard.[8] The pressure drop $\Delta p' = p'_1 - p'_2$ over the orifice without losses can be expressed as:

$$\Delta p' \approx \rho_0 \frac{1}{\sigma} l_e \frac{\partial u'}{\partial t} \; . \tag{5}$$

The losses caused by friction at the orifice walls, which are not considered in the above equation, can be included by an appropriate real valued constant R_l (see, e. g., Keller and Zauner [9]). For higher velocities, the flow separates at the edges of the orifice, which leads to additional losses. The velocity in the orifice can be expressed as $u'_o = 1/(C_d \, \sigma) \, u'$, where the contraction factor C_d accounts for the contraction of the flow due to the separation. If it is assumed that the kinetic energy of the flow in the orifice $1/2 \, \rho_0 \, (1/(C_d \sigma) \, u')^2$

American Institute of Aeronautics and Astronautics

is fully dissipated and does not recuperate downstream of the orifice (see for instance Ingard[4]), it follows

$$\Delta p' \approx \underbrace{\rho_0 \frac{1}{\sigma} l_e \frac{\partial u'}{\partial t}}_{\text{inertia}} + \underbrace{R_l \, u'}_{\text{viscosity}} + \underbrace{\frac{1}{2}\rho_0 \frac{u' \, |u'|}{(C_d \, \sigma)^2}}_{\text{flow separation}} \;. \tag{6}$$

It can be seen in the expression above that the loss terms due to friction and flow separation contribute to the resistive part. When the losses and the pressure drop are not in equilibrium, the fluid in the orifice is accelerated, which impacts solely the reactance of the transfer impedance $(\widehat{\partial u'/\partial t} = i\,\omega \hat{u})$.

In analogy, an acoustically compact area jump, as sketched in Fig. 2(b), can be considered for the investigation of a quarter wave resonator. By integration of the Bernoulli equation (3), the additional term $1/2\rho_0 \, u'^2 (1/\sigma^2 - 1)$ appears due the non-equal cross section area on both sides. In this case, the pressure drop can be expressed as:

$$\Delta p' \approx \rho_0 \frac{1}{\sigma} l_e^{AJ} \frac{\partial u'}{\partial t} + \frac{1}{2}\rho_0 \, u'^2 \left(\frac{1}{\sigma^2} - 1\right) + R_l^{AJ} \, u' + \frac{1}{2}\rho_0 \frac{u' \, |u'|}{(C_d \, \sigma)^2} \;. \tag{7}$$

Above, l_e^{AJ} and R_l^{AJ} denote a suitable effective length and linear loss term for the area jump, respectively.

III. Scattering to Higher Harmonics Described by Quasi-Steady 1-D-Analysis

In contrast to linear systems, nonlinear systems can respond not only at the fundamental frequency f_0 of the excitation, but also at its multiples, the so-called *higher harmonics*. The content of the fundamental frequency f_0 is referred to as the 1st harmonic, any multiples $n\,f_0$ as the nth harmonic ($n \in \mathbb{N}$). In the following, the spectrum of the response is studied numerically in dependency on the excitation frequency and amplitude. To the authors' knowledge, this is studied for the first time for resonator configurations in detail. The orifice, which is from a geometrical point of view close to the Helmholtz resonator, has been investigated with respect to its scatter behavior experimentally and analytically, see, e. g., Ingard and Ising[3,4] and Cummings.[5] A pattern in the harmonics has been observed in those studies, where the odd harmonics (3rd, 5th, . . .) dominate clearly over the even ones (2nd, 4th, . . .). This pattern is referred to as OHO ("Odd-Harmonics-Onl ') in the following. Ingard[4] and Cummings[5] explained the occurrence of the OHO pattern by studying quasi-steady 1-D equations.

In the following, these considerations are extended step by step to account also for an asymmetric orifice and for an area jump as they are present for a Helmholtz resonator with asymmetric neck and a quarter wave resonator. This analysis is applied to predict the relative contributions of the first five harmonics for Helmholtz resonators with symmetric and asymmetric neck as well as quarter wave resonators.

The occurrence or absence of the OHO pattern can be explained by studying quasi-steady 1-D equations as Eqs. (6) and (7). Similar considerations have been done by Ingard[4] and Cummings.[5] This theory presented in the literature is restricted by the assumption of a time-invariant contraction factor C_d for the whole cycle.

In the current study, the contraction coefficient C_d is assumed to be constant during the inflow and outflow half-cycle:

$$C_d = \left\{ \begin{array}{ll} C_d^+, & \text{for } u' \geq 0 \\ C_d^-, & \text{for } u' < 0 \end{array} \right. \;. \tag{8}$$

First, the nonlinear contribution of the pressure drop at an orifice is considered. Only the nonlinear term $\rho_0/[2(C_d \, \sigma)^2] \, u' \, |u'|$ in Eq. (6) contributes to the scattering to higher harmonics. Thus, the other terms are neglected in the analysis, i. e.,

$$\Delta p'(t) \frac{2\sigma^2}{\rho_0} = \frac{1}{C_d^2} \, u' \, |u'| \;. \tag{9}$$

If a sinusoidal velocity $u'(t) = A_u \sin(\omega_0 t)$ with frequency $f_0 = \omega_0/(2\pi)$ is assumed, the Fourier series of this pressure drop reads as

$$\Delta p'(t) \frac{2\sigma^2}{\rho_0 A_u^2} = \frac{a_0}{2} + \sum_{n=1}^{\infty} a_n \cos(n\omega_0 t) + b_n \sin(n\omega_0 t) \tag{10}$$

American Institute of Aeronautics and Astronautics

with the constants

$$a_n = \begin{cases} \frac{1}{2}(C_d^+ - C_d^-), & \text{for } n = 0 \\ \frac{1}{4}(C_d^- - C_d^+), & \text{for } n = 2 \\ 0, & \text{else} \end{cases} \tag{11}$$

and

$$b_n = \begin{cases} \frac{-4(C_d^- + C_d^+)}{\pi(n^3 - 4n)}, & \text{for odd } n \\ 0, & \text{else} \end{cases} \tag{12}$$

It can be seen that, for a symmetric configuration with $C_d^+ = C_d^-$, $a_n = 0$ for all n. Thus, only contributions with $b_n \neq 0$ remain for odd n. It can be concluded that the occurrence of the OHO pattern is due to the symmetry of the flow.

This flow symmetry is broken for an asymmetric orifice and for an area jump. During the inflow phase and with sufficient high amplitudes, the flow will contract, i. e., $C_d^+ < 1$. However, the flow does not contract when it jets out of the quarter wave, i. e., $C_d^- \approx 1$.

Due to the change in cross section at the area jump, an additional term appears in Eq. (7). This term can be expressed as:

$$\frac{1}{2}\rho_0 A_u^2 \sin^2(\omega_0 t)\left(\frac{1}{\sigma^2} - 1\right) = \frac{1}{4}\rho_0 A_u^2 \left(\frac{1}{\sigma^2} - 1\right)(1 - \sin(2\omega_0 t)) . \tag{13}$$

The expression above contributes significantly to the 2nd harmonic and, thus, amplifies the disappearance of the OHO pattern.

The following conclusions can be made from the considerations above: The Helmholtz resonator with symmetric neck shows the OHO pattern, where the harmonics decrease with increasing order. If its neck is asymmetric (e. g., with $C_d^+ \approx 0.95$ for sharp edged and $C_d^- \approx 0.7$ for $45°$ chamfered edge, see reference 10), the OHO pattern gets weaker. The 3rd harmonics is still dominant. But now the 2nd harmonics is predicted to be more pronounced than the 5th one. When a quarter wave resonator is considered, strong scattering in the 2nd harmonic is expected. The proportion of the scattering is here (for $\sigma \ll 1$) much larger than in the case of a Helmholtz resonator.

IV. Scattering to Higher Harmonics Observed in CFD Simulations

In this section, the predicted patterns in the amplitudes of the higher harmonics are verified and quantified with compressible CFD simulations for the three configurations considered. In theses simulations, a sinusoidal acoustic incoming wave $f = A_f \sin(\omega_0 t)$ at the excitation frequency $f_0 = \omega_0/(2\pi)$ is imposed at the inlet boundary. The response of the resonator is measured in terms of the reflected g wave, see Fig. 1. When scattering to higher harmonics occurs, it is accordingly present in this reflected g wave. The amplitudes of the higher harmonics $\hat{g}(n f_0)$ normalized by the amplitude of the fundamental harmonic of the incoming wave $\hat{f}(f_0)$ can be written as:

$$\frac{|\hat{g}(n f_0)|}{\left|\hat{f}(f_0)\right|} . \tag{14}$$

In the graphs presented in this section, the amplitude of the higher harmonics is always presented in this way. Neither the pressure nor the velocity in front of the resonator follow a strict sinusoidal function, since the reflected wave g influences both of these quantities with its higher harmonics.

In the analysis of the previous Sec. III, a sinusoidal velocity $u'(t) = A_u \sin(\omega_0 t)$ has been assumed. The higher harmonics occur there solely in the pressure drop $\Delta\hat{p}(n f_0)$. The amplitude of the nth harmonic can be normalized by the fundamental harmonic $\Delta\hat{p}(f_0)$, such that this harmonic is represented as

$$\frac{|\Delta\hat{p}(n f_0)|}{|\Delta\hat{p}(f_0)|} . \tag{15}$$

Accordingly, a quantitative comparison between the incompressible considerations and the compressible simulations is not possible. A qualitative comparison of compressible Helmholtz resonator simulations and incompressible orifice simulations is presented at beginning of Sec. IV.B. Before that comparison, the considered computational setup is introduced in Sec. IV.A. Finally, the results of the compressible simulations of three resonators are presented in Sec. IV.B.

American Institute of Aeronautics and Astronautics

Table 1. Geometric properties of the considered Helmholtz and quarter wave resonators.

	l_0 [mm]	d_0 [mm]	l_{cav} [mm]	d_{cav} [mm]	σ [%]	l_{ch} [mm]
HRS	4.0	4.2	20	50	0.71	0
HRA	4.0	4.2	20	50	0.71	0.35
QW	143	6.35	–	–	1.56	–

IV.A. Simulation Setup and Definition of the Test Cases

IV.A.1. Definition of Test Cases

In the present numerical study, a quarter wave resonator (QW) as well as Helmholtz resonators with symmetric (HRS) and asymmetric neck (HRA) are considered. The generic geometries are sketched in Fig. 1. For the Helmholtz resonators, the lengths and diameters of the neck and of the backing volume are denoted by l_0, d_0, l_{cav}, and d_{cav}, respectively. The neck of configuration HRA is chamfered by $45°$ on the outside with a length in axial direction of $l_{\mathrm{ch}} = 0.35\,\mathrm{mm}$. The length and diameter of the quarter wave resonator are named as l_0 and d_0. The values of those quantities are listed in Tab. 1. Configuration HRS is set as in reference 11 to have access to validation data. The chamfer length is set small enough that it influences the linear response of the resonator only marginally.

IV.A.2. CFD Solver Setup

Compressible CFD simulations are performed with the PIMPLE algorithm of OpenFOAM.[12] The slip condition is applied at the cylindrical wall of the impedance tube and the no-slip condition is used at the resonator itself, see Fig. 1. At the inlet, the *Navier-Stokes characteristics boundary condition* (NSCBC), cf. Poinsot and Lele,[13] is utilized. This boundary condition ensures a low acoustic reflection of the outgoing g wave. Simultaneously, an excitation signal can be imposed for the incoming f wave, which set sinusoidally $f = A_f \sin(\omega_0 t)$ with different fundamental frequencies $f_0 = \omega_0/(2\pi)$. At this inlet plane, the fluctuating pressure p' and velocity u' are monitored. From these quantities, the time series of the f and g waves can be computed directly. As explained above, the incoming wave scatters in the harmonics of the reflected wave $\hat{g}(n f_0)$ and is presented in following figures as defined in Eq. 14. In the post-processing, the transient parts of the data series have been removed and then truncated to a multiple of the period T to avoid leakage in the spectra. For further detail, on the solver refer to references 11. The simulations use 3-D meshes of at least 1.5 million cells.

The compressible CFD simulations are performed as large eddy simulation (LES) with the k-equation eddy-viscosity model as subgrid scale (SGS) model. Several SGS models have been tested. However, the acoustic response of the resonator depends only very weakly on the SGS modeling. Vortex structures are formed in the vicinity of the resonator neck due to the pulsation forcing of the flow. The dissipation to thermal energy of these vortices follows mainly the turbulent cascade. However, the separation process itself, responsible for the nonlinear acoustic dissipation, is almost not influenced by the vortices. This can also be seen with the Reynolds number based on the orifice size and velocity amplitude at the orifice, which remains rather low (maximum Re$\approx$ 3000 at 119.7 dB for HRS). Accordingly, the impact of the SGS model on acoustic properties remains very small as the separation process at the edges is resolved sufficiently. Moreover, comprehensive parameter studies regarding mesh, time-step, and solver parameters have been performed to ensure that the presented results are independent of the numerical settings. The solver has been validated in detail in the linear regime for various configurations in reference 11. In the nonlinear regime, the solver is validated against measurements of M. A. Temiz[14] based on a describing functions for configuration HRS, see Appendix.

To compare the simulation with a measurement, the input amplitude A_F of the f waves must be set such that the superposition of f and reflected $g = Rf$ wave matches the desired SPL, see reference 6 for more details. This requires an a priori knowledge of the reflection coefficient or an iterative process. In the following, this approach of setting the input amplitude is solely used for validation purposes. Besides that, the SPL is set only with respect to the input signal f ignoring the reflected acoustic g wave. This will be referred as to as *input SPL* in the following. Note that the input SPL and the actual SPL differ from each other.

American Institute of Aeronautics and Astronautics
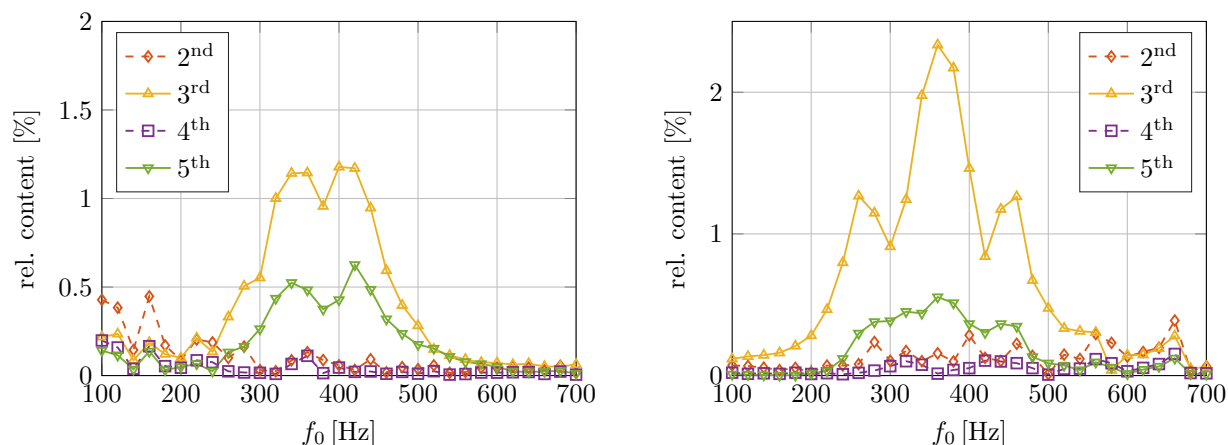
(a) Higher harmonics in f for the Helmholtz resonator (cf. Eq. (14)).

(b) Higher harmonics in $\Delta p'$ at the orifice (cf. Eq. (15)).

Figure 3. Higher harmonics for the Helmholtz resonator and the corresponding orifice with an excitation corresponding to a SPL of $119.7\,\text{dB}$.

For the orifice configuration, also incompressible simulations are performed with the SIMPLE algorithm of the commercial software ANSYS Fluent v15. A detailed description of the corresponding solver setting can be found in reference 6. Since the nonlinear behavior is linked to the magnitude of the velocity in the neck, the input amplitude has to be set such that velocities in the orifice and the neck agree.

IV.B.   Numerical Results

IV.B.1.   Validation via CFD of the Assumptions Made in the Theory Part

The analytical considerations of Sec. III are based on the assumption that the nonlinear mechanisms are similar for the Helmholtz resonators treated compressibly and the orifice treated incompressibly. Due to the different perspectives of the simulations (compressible vs. incompressible), a direct qualitative comparison between those setups is not possible, as mentioned above. Figure 3 shows the spectral response of both a resonator (compressible simulation) and of the corresponding orifice (incompressible simulation). In the compressible simulations, the input amplitudes A_f of the f wave is set in a way that a SPL of $119.7\,\text{dB}$ is achieved at the reference distance $l_{ref} = 49.7\,\text{mm}$ in front of the resonator. The amplitude A_u of the velocity in the incompressible simulations is adjusted such that the velocities in the resonator neck and the orifice coincide. Qualitatively, the results for the two setups agree well. Both exhibit the OHO pattern and the same ordering of the odd harmonics. The scattering to higher harmonics takes place close to the eigenfrequency $f_{\text{res}} \approx 380\,\text{Hz}$, where the velocities are largest in the neck and orifice, respectively. This comparison underlines that the quasi-steady analysis of Sec. III of the acoustically compact elements describes also the main mechanisms at the compressible resonators correctly.

Before the scattering to higher harmonics in the compressible CFD simulations for each resonator is discussed, the flow contraction is investigated for these configurations. In Fig. 4, a snapshot of the flow field during the inflow and outflow phase for all configurations is presented. These snapshots are cropped to the vicinity of the resonator neck and mouth, respectively. The separation zones are marked in green at the upper edges in each figure. The resonators are excited at $380\,\text{Hz}$ with an input SPL of $125\,\text{dB}$ (for HRS and HRA) and at $580\,\text{Hz}$ with $160\,\text{dB}$ (for QW), which is close to the corresponding resonator eigenfrequency. As explained above, these SPL values are set here and in the following as input SPLs, which means that the SPL values refer solely to the input f waves while ignoring the reflected g waves. The separation behavior is similar for the inflow and outflow for HRS, see Figs. 4(a) and 4(b). A contraction ratio of ≈ 0.7, as can be found in the literature,[10] is confirmed by the simulation. The asymmetric neck induces an asymmetric separation behavior. During the outflow, the contraction remains the same as for HRS, see Fig. 4(d). However, the flow contracts less with a factor $C_d^+ \approx 0.9$ for the inflow (Fig. 4(c)), which is close to literature values (0.95 in Blevins' textbook[10]). The separation is also asymmetric for the quarter wave resonator QW

American Institute of Aeronautics and Astronautics

(a) HRS inflow.

(b) HRS outflow.

(c) HRA inflow.

(d) HRA outflow.

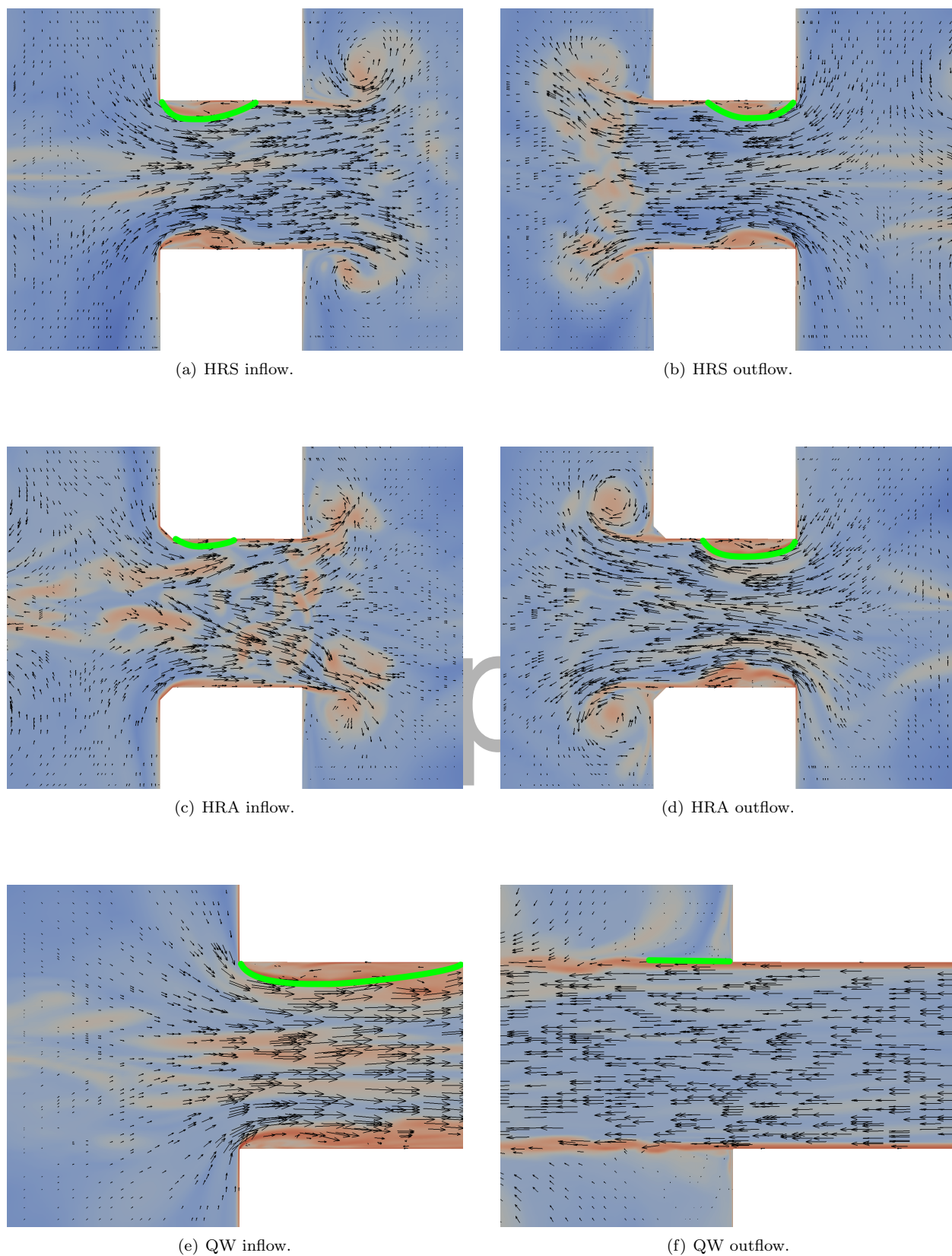(e) QW inflow.

(f) QW outflow.

Figure 4. Flow visualization in a 2-D cutting plane in the vicinity of the resonator neck/mouth during the inflow and outflow phases for the three configurations considered at excitation frequency close to the eigenfrequency ($f_0 = 380\,\text{Hz}$ with input SPL $125\,\text{dB}$ for HRS and HRA, $f_0 = 580\,\text{Hz}$ with input SPL $160\,\text{dB}$ for QW). On the upper half, the contraction is mark in green for each case.

American Institute of Aeronautics and Astronautics

with $C_d^+ \approx 0.7$ and $C_d^- \approx 1$ as can be seen in Figs. 4(e) and 4(f). Overall, it can be concluded that the assumption of Sec. III that the contraction depends on the flow direction is reasonable.

IV.B.2.   *Scattering to Higher Harmonics at the Helmholtz Resonator with Symmetric Neck*

The amplitudes of the higher harmonics nf_0 up to order $n = 5$ of the resonator response for an input SPL of 125 dB are plotted in Fig. 5(a) for the fundamental, excitation frequency f_0 in the range of [200 - 700] Hz. All harmonics with larger order ($n > 5$) are negligible with a relative content of $< 2\,\text{‰}$. It can be observed that scattering mainly occurs close to the eigenfrequency, i. e., at $f_0 \approx f_{\text{res}}$. This is in line with expectations since the velocity in the neck is largest in this frequency range and is causing strong nonlinear effects here. Away from the eigenfrequency, velocities are smaller and the system behaves almost linearly. As expected, the OHO pattern occurs, i. e., the odd harmonics contribute predominantly to the response, while the even harmonics are almost absent. The 3$^{\text{rd}}$ harmonic ($—\triangle—$) clearly dominates over the even ones (2$^{\text{nd}}$ ($-\diamond-$) , 4$^{\text{th}}$ ($-\square-$) , . . .). The contribution of the harmonics becomes less and less considerable with increasing order n. The impact of the 5$^{\text{th}}$ harmonic ($—\triangledown—$) is noticeably smaller than the 3$^{\text{rd}}$ but is still more prominent than even harmonics.

In Fig. 5(b), the scattering to higher harmonics is depicted under variation of the input SPL for an excitation frequency $f_0 = 380$ Hz, which is close to the eigenfrequency f_{res}. The reflection coefficient and the resistance are presented in Fig. 6 ($—\triangle—$). Note that the reflection coefficient equals the scattering into the fundamental harmonic. With increasing input SPL, the fundamental harmonic first decays (up to 110 dB), since the resistance increases, see Fig. 6(b). The optimal damping for orthogonal incident acoustic waves is achieved with a normalized impedance $z = 1$. Increasing the excitation further leads to higher resistance, but also the reflection increases. This occurs due to the over-damping of the system.

The scattering to higher harmonics increases with increasing amplitude in the normal-damped range ($z < 1$). Close to the region of optimal damping ($z = 1$), the scattering to higher harmonics attains abruptly a local minimum. This minimum cannot be explained with the analysis of Sec. III, since the velocity in the neck is actually further increasing. Furthermore, the scattering to higher harmonics does not totally vanish for low amplitudes. The considerations made above would actually suggest a monotonic increase of the scattering with the amplitude, starting with no scattering and reaching asymptotically a limit. The reasons for the discrepancy to the presented simulation results are still unknown. In the over-damped range, the scattering increases again by increasing the input SPL. The overall scattering remains small for this resonator setup even for very high excitation levels. Thus, modeling the nonlinear behavior only for the fundamental frequency f_0 with the describing function approach (see Sec. II.A) reflects the main mechanism accurately in that case.

It can be observed that the OHO pattern vanishes in a range of very high SPL (≥ 130 dB), which is shaded in gray in Figs. 5(b) and 5(d) (for HRA). The interaction of the vortices formed at leading and trailing edges was identified as the cause of this behavior. The exact mechanism and the circumstances when the OHO pattern is absent will be discussed in detail in a separate article.[15]

### IV.B.3.   *Scattering to Higher Harmonics at the Helmholtz Resonator with Asymmetric Neck*

The gain of the reflection coefficient and resistance for various SPLs are included in Fig. 6 for the configuration with the asymmetric neck HRA. The chamfer size has been set such that the linear impedance is almost not influenced by the chamfer. Thus, the eigenfrequency remains the same as for HRS and the excitation for that case is also set to 380 Hz. The nonlinear resistance can be observed to decrease slightly in comparison to the unchamfered case HRS, see Fig. 6(a). This decrease arises from the lower flow contraction during the outflow phase, see reference 11. The higher harmonics nf_0 are shown for an input SPL of 125 dB in Fig. 5(c) for a range of [200 – 700] Hz for the fundamental, excitation frequency f_0. Moreover, the scattered higher harmonics are presented for an excitation of 380 Hz with varying input SPL in Fig. 5(d). As predicted, the 2$^{\text{nd}}$ harmonic increases in comparison to HRS with symmetric neck. According to the analysis of Sec. III, the 2$^{\text{nd}}$ harmonic should be weaker than the 3$^{\text{rd}}$ but stronger than the 5$^{\text{th}}$ one. However, the increase of the 2$^{\text{nd}}$ harmonic is moderate such that the 2$^{\text{nd}}$ and 5$^{\text{th}}$ harmonics have about an equal strength in the CFD simulations.
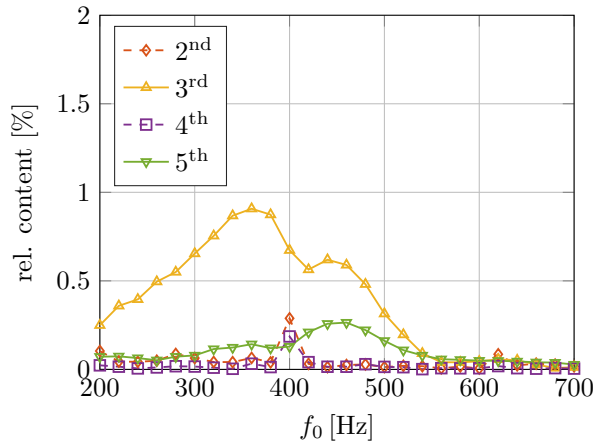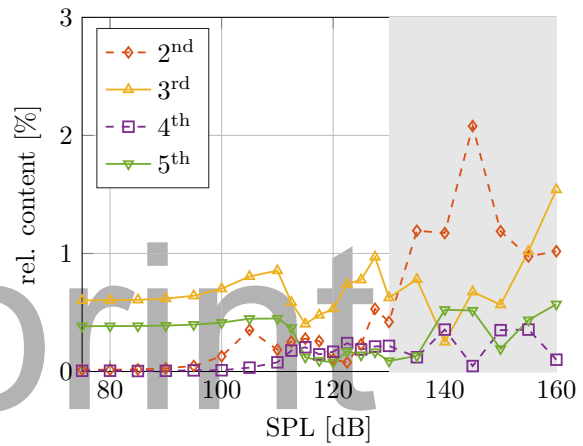
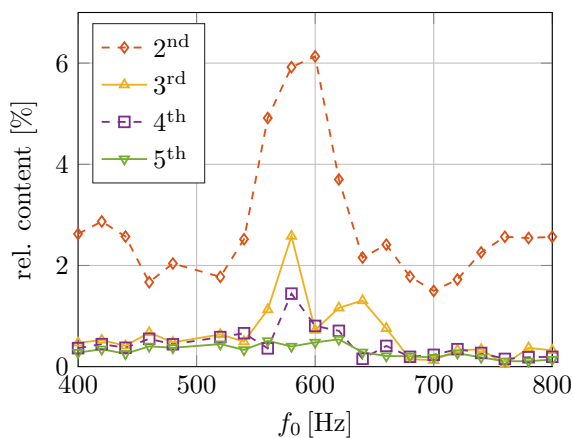(a) Helmholtz resonator HRS for input SPL 125 dB.
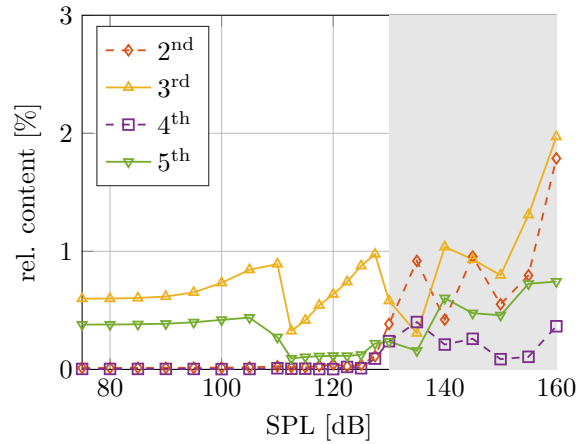
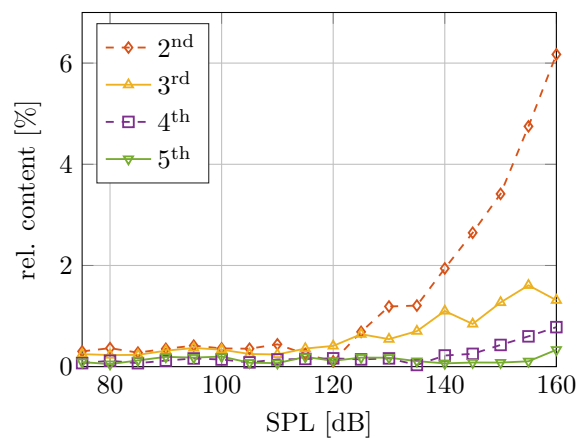(b) Helmholtz resonator HRS at 380 Hz for variable input SPL.
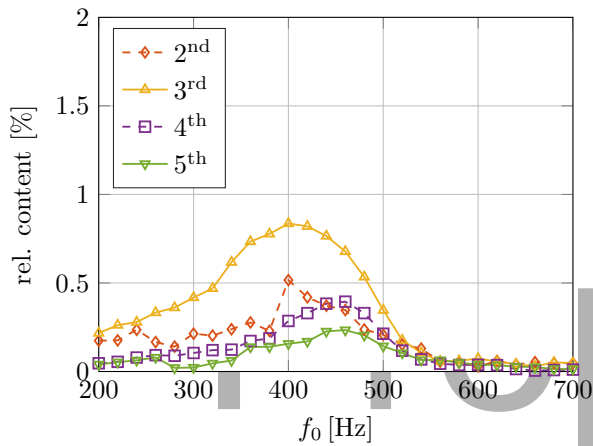
(c) Helmholtz resonator with asymmetric neck HRA for input SPL 125 dB.

(d) Helmholtz resonator with asymmetric neck HRA at 380 Hz for variable input SPL.

(e) Quarter wave resonator QW for input SPL 160 dB.

(f) Quarter wave resonator QW at 580 Hz for variable input SPL.

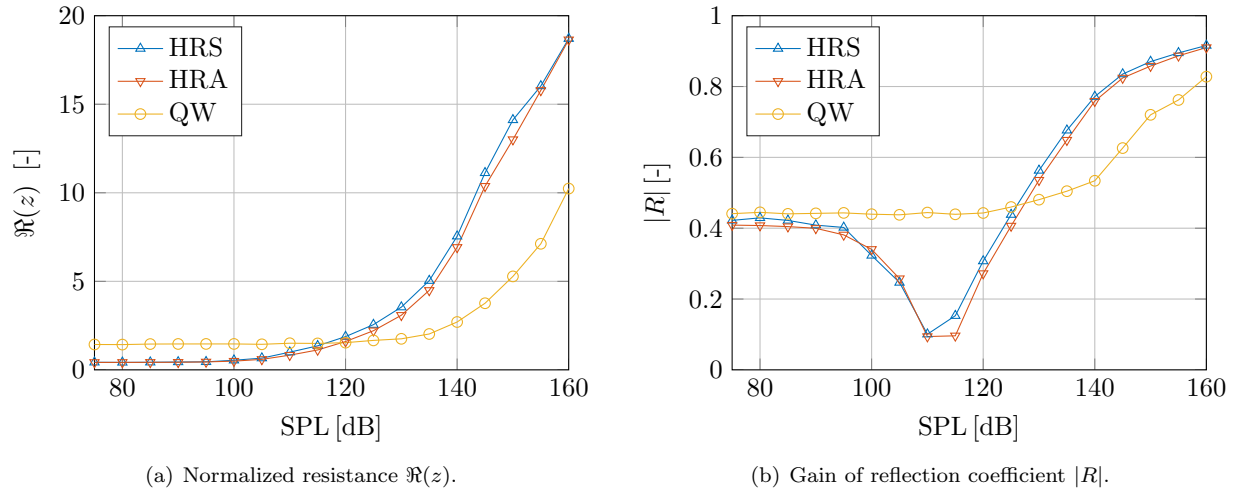Figure 5. Spectra of the acoustic responses for the three geometries considered.

American Institute of Aeronautics and Astronautics

(a) Normalized resistance $\Re(z)$.

(b) Gain of reflection coefficient $|R|$.

Figure 6. Gain of reflection coefficient $|R|$ and normalized resistance $\Re(z)$ under variation of the input SPL at the corresponding eigenfrequency ($f_0 = 380\,\text{Hz} \approx f_{\text{res}}$ and $f_0 = 580\,\text{Hz} \approx f_{\text{res}}$, respectively) for the three configurations considered.

IV.B.4.   *Scattering to Higher Harmonics at the Quarter Wave Resonator*

For the quarter wave resonator, the behavior changes significantly with respect to the Helmholtz resonators. For QW, the scattering is mostly into the 2nd harmonic, which again fits well to the analysis of Sec. III. This can be seen in Fig. 5(e) for a constant SPL of 160 dB and in Fig. 5(f) for the eigenfrequency $f_0 = 580\,\text{Hz} \approx f_{\text{res}}$ in a range of $[75 - 160]$ dB. The frequency sweep is performed for QW at 160 dB instead of 125 dB as for Helmholtz resonator configurations due to the higher SPL required to trigger nonlinear behavior. This can be seen in Fig. 6(a) (——). For HRS, the resistance starts to increase at a SPL of about 105 dB due to nonlinear effects. For QW, this occurs at about 125 dB. This difference can be explained only partially due to the different open area ratios σ. Thus, the different threshold to trigger nonlinearities originates mainly due to the different resonator concepts. Moreover, the overall scattering increased as well. The maximal scattering was in the order of 2 % for the Helmholtz resonators. Here for QW, the relative scattering to the 2nd harmonic can reach values up to the order of 10 %. This difference in magnitude of the Helmholtz and the quarter wave resonator is backed by the quasi-steady analysis.

V.   Summary and Conclusion

The nonlinear acoustic response of quarter wave and Helmholtz resonators has been studied by means of compressible CFD simulations. Particular attention was paid to the scattering to higher harmonics. For the Helmholtz resonators the higher harmonics exhibit an odd-harmonics-only (OHO) pattern, where only the odd harmonics are present, while the even ones are negligible. Such patterns were observed previously at symmetric orifices, and explained by a 1-D quasi-steady analysis based on the Bernoulli equation with suitable extra terms for the losses.[3–5] The current study extends the analysis, such that it is applicable also to configurations that exhibit asymmetric flow patterns, e.g. Helmholtz resonators with an asymmetric necks, or quarter wave resonators.

The following observations are observed in CFD simulations and confirmed by the quasi-steady analysis: For the Helmholtz resonator with a symmetric neck, the scattering to higher harmonics exhibits the OHO pattern. The OHO pattern is weaker if a Helmholtz resonator with an asymmetric neck is considered. It is concluded that the pure OHO pattern occurs due to the flow symmetry during the inflow and outflow phase through the symmetric resonator neck. For the quarter wave resonator – corresponding to a simple discontinuity in cross-sectional area in the 1-D compact analysis – a larger threshold for the excitation is required to trigger noticeable nonlinear effects. If scattering takes place in this configuration, the 2nd harmonic is the dominant higher harmonic, and the OHO pattern vanishes completely.

Overall, the scattering to higher harmonics is more pronounced for the quarter wave resonator, for which values up to the order of 10 % of the incident wave are observed. In contrast, Helmholtz resonators exhibit

American Institute of Aeronautics and Astronautics

(a) Normalized resistance $\Re(z)$.

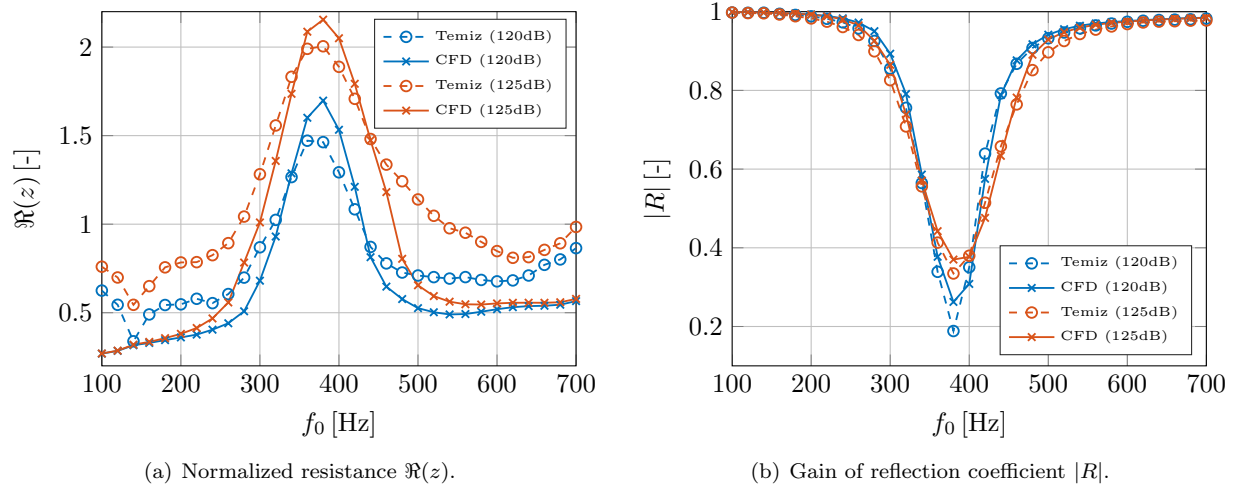(b) Gain of reflection coefficient $|R|$.

Figure 7. Impedance and reflection coefficient for HRS with SPLs of about 120 dB and 125 dB indicated by different colors. Measurements of M. A. Temiz[14] are plotted as solid lines, simulation results as circles.

quite moderate nonlinear scattering (up to 2 %) even for very high excitation levels. One may conclude that in many cases describing functions for impedance or reflection coefficient characterize the nonlinear response of resonators with acceptable accuracy.

Appendix

The solver validation in the nonlinear regime is presented using impedance describing function measurements performed by M. A. Temiz from TU Eindhoven on configuration HRS. Since the nonlinear effects affect mainly the resistance $\Re(z)$, it is more challenging to capture this quantity correctly in the CFD simulation than reactance $\Im(z)$, which always fit very accurate. Figure 7(a) presents the normalized resistance $\Re(z)$ for the two SPLs obtained with CFD simulations and for measurements.[11] Here, the input amplitudes of the f wave have been set in a way that the acoustic SPL directly in front of neck matches the target value. The curves agree quite reasonably but the numerics slightly over-predicts the nonlinear resistance. The measurements are also a bit shaky away from the eigenfrequency. This shaky behavior does not originate from physics but from the ill-conditioned transformation from reflection coefficient to resistance. The reflection coefficient is in both experiment and CFD the quantity that is directly and subsequently transformed to the impedance. Thus, a comparison in the reflection coefficient is more valid. This is depicted in Fig. 7(b) for the gain of this coefficient (which is again more difficult to capture than its phase). Here, the curve match is almost perfect and shows the quality of the computational setup.

Acknowledgments

References

[1] A. S. Hersh, B. E. Walker, and J. W. Celano. Helmholtz Resonator Impedance Model, Part 1: Nonlinear Behavior. *AIAA J.*, 41(5):795–808, 2003.

[2] A. S. Hersh and B. Walker. Fluid Mechanical Model of the Helmholtz Resonator. *NASA Tech. Report*, NASA-CR-2904, 1977.

American Institute of Aeronautics and Astronautics

[3] U. Ingard and H. Ising. Acoustic Nonlinearity of an Orifice. *J. Acoust. Soc. Am.*, 42(1):6–17, 1967.

[4] U. Ingard. Nonlinear Distortion of Sound Transmitted through an Orifice. *J. Acoust. Soc. Am.*, 48(1A):32–33, 1970.

[5] A. Cummings. Transient and multiple frequency sound transmission through perforated plates at high amplitude. *J. Acoust. Soc. Am.*, 79(4):942–951, 1986.

[6] J. Tournadre, K. Förner, P. Martínez-Lera, and W. Polifke. Determination of acoustic impedance for Helmholtz resonators through incompressible unsteady flow simulations. In *22nd AIAA/CEAS Aeroacoustics Conference*, Lyon, France, 2016.

[7] S. W. Rienstra and A. Hirschberg. An Introduction to Acoustics. Technical Report IWDE 92-06, Eindhoven University of Technology, 2015.

[8] U. Ingard. On the Theory and Design of Acoustic Resonators. *J. Acoust. Soc. Am.*, 25(6), 1953.

[9] J. J. Keller and E. Zauner. On the use of Helmholtz resonators as sound attenuators. *Z. Für Angew. Math. Phys.*, 46:297–327, 1995.

[10] R. D. Blevins. *Applied Fluid Dynamics Handbook*. Van Nostrand Reinhold, NY, 1984.

[11] K. Förner, M. A. Temiz, W. Polifke, I. Lopez Arteaga, and A. Hirschberg. On the Non-Linear Influence of the Edge Geometry on Vortex Shedding in Helmholtz Resonators. In *22nd International Congress on Sound and Vibration (ICSV22)*, Florence, Italy, 12 - 16 July 2015.

[12] OpenFOAM Foundation. OpenFOAM (Version 2.3.0) [software]. February 2014.

[13] T. Poinsot and S. K. Lele. Boundary conditions for direct simulation of compressible viscous flows. *J. Comp. Phys.*, 101(1):104–129, 1992.

[14] M. A. Temiz. Private measurement data exchange, 2016.

[15] J. Tournadre, K. Förner, W. Polifke, P. Martínez-Lera, and W. Desmet. Influence of vortex disruption on the nonlinear acoustic response of orifices. *submitted to: JSV*, 2006.

Preprint

American Institute of Aeronautics and Astronautics